IOP Publishing Smart Materials and Structures
Smart Mater. Struct. **30** (2021) 095005 (10pp) https://doi.org/10.1088/1361-665X/ac15a1

3D-printed liquid metal-based stretchable conductors and pressure sensors

Thassyo Pinto[1,*], Claudia Chen[2], Cody Pinger[3] and Xiaobo Tan[1,2]

[1] Department of Electrical and Computer Engineering, Michigan State University, East Lansing, MI 48824, United States of America
[2] Department of Mechanical Engineering, Michigan State University, East Lansing, MI 48824, United States of America
[3] Institute for Quantitative Health Sciences and Engineering, Michigan State University, East Lansing, MI 48824, United States of America

E-mail: thassyo@msu.edu

Received 10 May 2021, revised 21 June 2021
Accepted for publication 18 July 2021
Published 29 July 2021

Abstract

Microfluidic devices control fluids on the micrometer-scale and are commonly used for lab-on-chip applications, such as sensors, micropumps and biological analyzers. Commonly reported fabrication methods for achieving flexible microfluidic structures are labor-intensive, require many cumbersome steps, and have limited options for materials. This paper presents a rapid-manufacturing technique using a PolyJet 3D-printer for creating soft microfluidic substrates embedded with liquid metals to fabricate stretchable conductors and pressure sensors. By using this novel method, several spiral-shaped soft pressure sensors with multimaterial-based substrates are 3D-printed simultaneously in less than six minutes. Microfluidic channels with cross-sections ranging from 150 $\times$ 150 to 350 $\times$ 350 μm are successfully achieved in a soft substrate. This 3D-printing method allows fabrication of complex, enclosed channels without any photocurable support material, thus minimizing post-processing time. Simulation and experiments are conducted to characterize the quasi-static and dynamic properties of the fabricated pressure sensor. In particular, experimental results show that these 3D-printed microfluidic pressure sensors are robust, capable of withstanding high pressures up to 1 MPa.

Keywords: soft robotics, liquid metals, 3D-printing, stretchable sensors

(Some figures may appear in colour only in the online journal)

1. Introduction

Microfluidics systems process or manipulate small amounts of fluids, using channels with dimensions of tens to hundreds of micrometers [1]. Several microfluidic structures have been applied extensively in many sensing applications, such as force detection [2, 3], strain gauges [4, 5], flow rate measurement [6], and noninvasive health analysis [7–9]. In the area of soft robotics, a variety of sensing modalities can be embedded in soft robotic structures and actuation mechanisms to provide feedback [10–13]. The most common methods for sensor measurement in soft robotics are resistive and capacitive technologies [14]. These sensors are often fabricated using nanoscale conductive materials deposited over a flexible substrate such as polydimethylsiloxane (PDMS) [15, 16].

The deformability and mobility of liquid metals (LMs) brings significant potential for soft robots and machines [17]. LM alloys, such as EGaIn (75.5 wt% gallium and 24.5 wt% indium) [18] and Galinstan (68.5 wt% gallium, 21.5 wt% indium, and 10 wt% tin) [19], have been explored for soft sensors due to their low melting point, excellent liquidity, high electrical conductivity, good thermal conductivity, low vapor pressure, and low toxicity in comparison to mercury. Some examples of LM-infused microfluidic sensors include

* Author to whom any correspondence should be addressed.

wearable soft sensors for human gait measurement [20, 21], soft gloves for hand motion detection [22], soft tactile sensors for force feedback in micromanipulation [23], and soft pneumatic actuators with embedded microfluidic sensing [24–26]. Patterning of liquid metals in 2D and 3D also allows the creation of metallic microstructures, stretchable conductors, and sacrificial templates for microfluidic channels [27–29].

Traditionally, microchannel structures for sensing devices are fabricated using labor-intensive and cumbersome methods. The literature in its majority has reported microchannel-based sensors by following fabrication techniques such as laser micromachining to create molds [30], vapor deposition of hydrophobic monolayers for easy demolding [31], spin coating of PDMS to create thin elastomer films [32], cross-linking of silicones through oven-curing [33], and oxygen plasma treatment to construct the microchannel cavities [34]. A liquid metal-based soft artificial skin was created using silicone casting over a 3D-printed mold [35]. Aside from many additional fabrication steps, the silicone curing process alone can take hours. Curvature sensors with microchannels filled with EGaIn have been produced using a combination of photolithography and replica molding [36]. However, the entire fabrication process including vapor deposition, silicone cross-linking, oxygen plasma treatment, and elastomer film bonding, is approximately four hours long. PDMS microchannel tiles in devices tailored to laser axotomy and long-term microelectrode arrays (MEA) can take more than two days for fabrication when using soft lithography procedures [37]. 3D-printing technology has also been explored to rapidly prototype microchannel structures, accelerating the research and development of microfluidic sensors and devices [38, 39]. However, 3D-printing process over soft substrates remains a challenge. For instance, some rapid manufacturing techniques, such as using polyethylene glycol (PEG) as a sacrificial layer through ink-jet printing, requires a 10 h long curing process of the PDMS-based substrate [40]. Modified photocurable materials have also been explored for 3D-printing of soft pressure sensors, but a custom-built printing system is required to develop these devices [41]. These previously reported methods present some disadvantages and challenges, such as time-consuming procedures, limited materials selection, difficulty in removing the sacrificial layer, and poor repeatability in fabrication.

In this paper, we present a novel easy and quick technique for fabricating flexible microchannels and subsequently, filling these channels with LMs to create stretchable conductors and soft pressure sensors. 3D-printed flexible substrates with microchannel structures are achieved by embedding a mixture of glycerol and isopropanol (IPA) as sacrificial support. This new rapid prototyping approach allows convenient manufacturing of multiple replicates within minutes. Microchannel substrates with different shapes (straight lines and spirals) and sizes are explored, and the lowest functional dimensions for straight microfluidic channels are determined to be 150 μm$\times$ 150 μm in cross-section. Spiral-shaped microchannels, with cross section of 350 μm $\times$ 350 μm, are further used to demonstrate stretchable pressure sensors, by manually injecting EGaIn after removal of the liquid support material. Experiments and simulation are conducted to characterize and understand quasi-static and dynamic responses of the sensor; in particular, experimental results show that the pressure sensors can withstand pressures up to 1 MPa.

The rest of the paper is organized as follows. In section 2, we describe the procedures for designing and fabricating 3D-printed microfluidic channels, conductors, and sensors. In section 3, simulation is conducted to estimate the average strain of the pressure sensor under a range of pressures relevant to experimental characterization. Experimental setup and characterization results for the pressure sensor are presented in section 4. Additional discussion on the methods and results are provided in section 5. Finally, concluding remarks and future research directions are presented in section 6.

2. Design and fabrication

2.1. Microchannel 3D-printing

The proposed method for fabricating microfluidic structures for stretchable conductors and pressure-sensing devices was inspired by the technique presented in [42], which investigated 3D-printing of enclosed microfluidic channels in *rigid* materials without photocurable support. The latter method utilizes a viscous liquid support instead, requiring minimal to no postprocessing to form sealed channels. In this work, we seek to extend this approach to soft substrates in order to achieve stretchable 3D-printable microchannel-based conductors and sensors. A PolyJet-based 3D-printer (J750, Stratasys) and a UV-cured resin with post-cured rubber-like properties (Agilus30, Stratasys) were used to create the microchannel cavities. This fabrication process followed a three-step procedure: 3D-printing the bottom substrate containing open microchannel cavities, filling the microchannel cavities with liquid support material, 3D-printing a top substrate layer directly onto the bottom substrate to close the microchannels. These steps can be repeated several times depending on the number of microchannel or substrate layers.

Traditionally, 3D-printing of devices with enclosed hollow channels requires initially printing the channel so that it is filled with a sacrificial photocurable support material. This material is then manually removed in post-processing, a procedure that can take hours to days; for small channels with complex geometries (e.g. spirals or serpentines), this process is not even possible. The method presented here allows fabrication of channels without any photocurable support material. The 3D geometry design for the microfluidic soft substrate was separated into two parts: a bottom layer with the microchannel cavities, and a top flat layer with holes at each end of the microchannel for removing the liquid support material. First, the soft substrate bottom layer was 3D-printed over a transparency film (Premium Transparency, Xerox) to facilitate the final substrate removal from the 3D-printer bed. Next, once the bottom layer printing process was finalized, a liquid sacrificial layer, composed of glycerol (Glycerol 99.5%, Sigma-Aldrich) and isopropanol (2-propanol 99.5%, Sigma-Aldrich) mixture

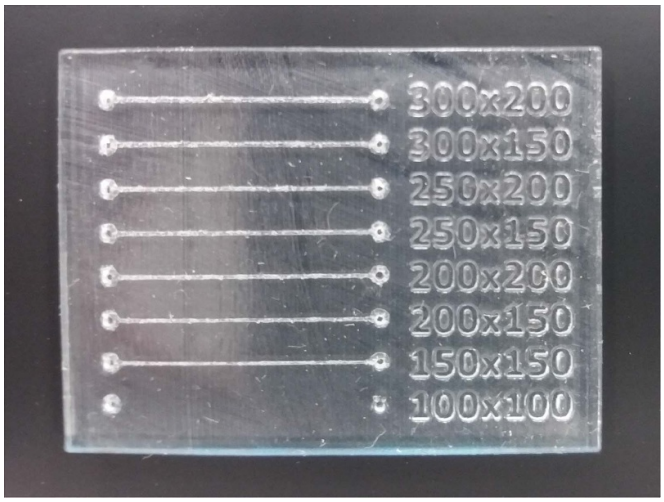

Figure 1. 3D-printed straight microchannels over a soft substrate (Agilus30) with 2 mm overall thickness. The minimum microchannel cross-section size identified was of 150 μm $\times$ 150 μm (height/width).

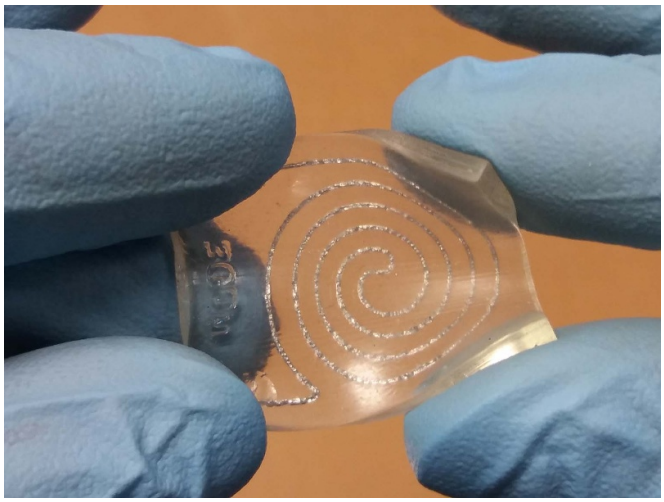

Figure 2. 3D-printed microfluidic spiral-shaped soft pressure sensor with embedded liquid metal (EGaIn).

(70:30 v:v), was manually dispersed over the microchannel cavities using an 1 ml plastic syringe. A small flexible spatula was used to distribute the mixture evenly throughout the exposed microchannels and remove any excessive glycerol-isopropanol solution. If removed properly, any remaining solution on the surface has negligible effects on the robustness of bonding between the channel layer and the top layer to be printed next [42], likely due to its mixing with the dispersed Agilus30/VeroClear during printing. In addition, during the liquid dispersion phase, the top layer printing process was already initialized, with the 3D-printer head performing automatic calibration outside the print bed for 30 s. This is an important process to avoid beading of the liquid support material between the layers, which could lead to clogging or irregular cavities. The entire printing process, including manual liquid dispersion, took approximately 6 min. This method was tested for fabricating up to six sensor substrates simultaneously.

As an initial investigation, we first created a 3D CAD model of a substrate with 2 mm overall thickness and multiple straight microchannels (SolidWorks, Dassault Systemes) to determine the minimum cavity cross-section height and width for 3D-printing microchannels into a soft material. We selected several dimensions based on reported results from literature regarding liquid conductor-based sensors [43, 44]. The width of the straight microchannels had a range from 300 μm down to 100 μm, and a height range from 200 μm down to 100 μm. As shown in figure 1, the smallest achievable microchannel had 150 μm $\times$ 150 μm cross-section.

2.2. Pressure sensor design

A microfluidic pressure sensor was developed by creating spiral-shaped microchannels within a soft substrate. This makes the sensor suitable for pressure detection, since it will not respond to uniaxial stretches within the plane due to counter-balanced electrical resistance change in perpendicular directions [33]. Although it was found that the minimal microchannel size for the fabrication technique in this work was 150 μm $\times$ 150 μm, this dimension presented challenges in the removal of the glycerol/IPA mixture from the inner cavities when designed as a spiral. We identified that a microchannel cross-section of 350 μm $\times$ 350 μm or larger would be suitable for the sensor design (figure 2).

The pressure sensor was designed with a substrate of dimensions 30 mm $\times$ 25 mm $\times$ 1.5 mm, with the spiral microchannel centered at the middle. The microchannel design was comprised of a three-turn spiral (inwards and outwards) with 1.3 mm spacing between channels and a total sensor active area of 20 mm in diameter. A mix ratio between Agilus30 and VeroClear materials was selected in order to balance the sensor compliance (70A durometer). The bottom layer and the cavity structure combined had a total height of 925 μm, and the upper layer had a thickness of 575 μm. The complete fabrication process is explained in figure 3.

2.3. Liquid metal embedding and encapsulation

The liquid metal used in this work was EGaIn, which had a high electrical conductivity ($\sigma = 3.4 \times 10^6$ S m^{-1}), a resistivity of $\rho = 29.4 \times 10^{-8}$ Ω m^{-1}, and low toxicity [45]. After completion of the 3D-printing process for the substrate, a small tubing connected to a vacuum pump was inserted into one of the microchannel ports to extract the glycerol mixture. The removal process only took approximately 3–5 s for each device. Once all the liquid support was removed, a 1 ml syringe with 22 gauge needle (0.70 mm) was used to inject the liquid-phase alloy (EGaIn, Sigma-Aldrich), composed of $\geqslant$99.9% trace metal basis, inside the microchannel cavities (figure 3(f)).

Uncured Agilus30 was initially used to encapsulate the open microchannel ports which were connected to thin copper wires. However, as reported in previous works [36], movement of the wires interfacing the LM in the microchannels caused

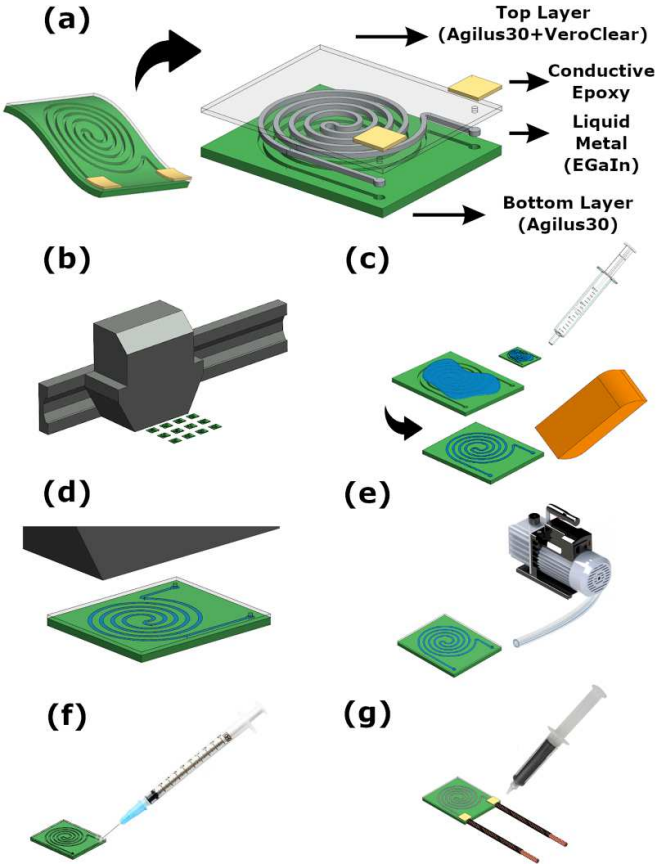

Figure 3. Design and fabrication steps of the 3D-printed pressure sensor embedded with LM. (a) The sensor components: a bottom layer made of pure Agilus30, a top layer made of Agilus30 and VeroClear mixture (70A Shore Hardness), a microchannel structure for filling with liquid metal (EGaIn), and two end terminals encapsulated with conductive epoxy; the fabrication steps were: (b) simultaneous 3D-printing of multiple pressure sensors starting by the bottom layer with microchannel cavities of cross-section size 350×350 μm, (c) manual dispersion of the glycerol-IPA mixture, (d) 3D-printing of the top layer with outlets at each end, (e) vacuum-based removal of liquid sacrificial layer, (f) manual injection of EGaIn, and (g) encapsulation of both terminals and soldering of copper stranded wires with conductive epoxy.

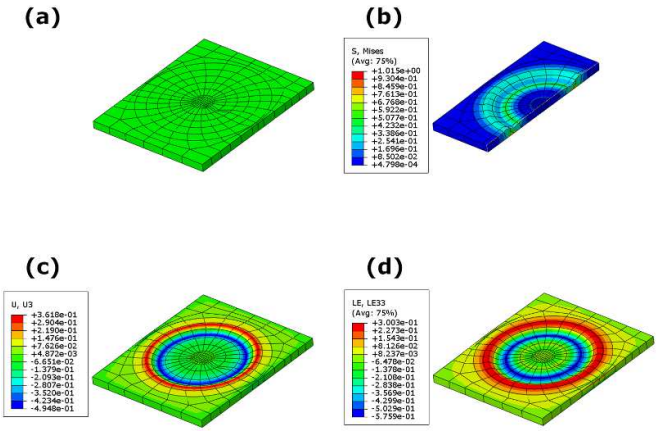

Figure 4. Contour plots of the simulated soft pressure sensor for an applied pressure of 1 MPa. (a) Substrate geometry meshed with hexahedral elements of type C3D20RH; (b) cut-view of the von Mises stress; (c) spatial displacement at z-direction; (d) logarithmic strain at z-direction.

measurement issues. Therefore, we explored an alternative method by sealing the microchannel ports with conductive epoxy (8331 Silver Conductive Epoxy Adhesive, MG Chemicals), and then gluing thick braided copper wires to each electrode with the same adhesive. To expedite the manufacturing procedure, a hot plate was used to speed up the adhesive curing process to 10 min at 70 °C. This allowed a robust bonding between soft and hard conductive materials.

3. Simulation of sensor under pressure

Finite elements analysis (FEA) of the 3D-printed soft pressure sensor device was carried out using a multiphysics software (Abaqus/CAE, Dassault Systemes). The simulation was conducted to understand the range of compressive strains experienced by the sensor, which will be instrumental in deriving the gauge factor of the sensor when the latter is viewed as a strain sensor (in the normal direction). A simple geometry representing the sensor substrate was created following the same physical dimensions. In this study, to facilitate computation, we considered the microchannel cavities and the liquid metal as solid but soft materials with similar properties as the substrate. The material property was set as Agilus30 using the Odgen hyperelastic model, with strain energy function

$$\Psi = \sum_{i=1}^{N} \frac{\mu_i}{\alpha i}(\lambda_1^{\alpha_i} + \lambda_2^{\alpha_i} + \lambda_3^{\alpha_i} - 3) \tag{1}$$

where μ is the shear modulus

$$\mu = \frac{1}{2}\sum_{i=1}^{N} \mu_i \alpha_i. \tag{2}$$

We used the simulation parameters $\mu_1 = 0.2127$ MPa, $\alpha_1 = 1.3212$, $\mu_2 = 0.0375$ MPa, $\alpha_2 = 4.318$, $\mu_3 = -0.001$, $\alpha_3 = -1.0248$, as determined in [46]. A pressure input of up to 1 MPa with increments of 0.1 MPa per step was applied. A fixed boundary condition was set on the bottom surface of the sensor to prevent planar rotation and displacement. The pressure was applied via the top surface, over an area defined by a circle with a diameter of 16 mm centered at the sensor active area, which replicates the experimental setup.

Figure 4 shows the obtained contour plots for von-Mises stress, displacement and logarithmic strain along the load axis. The average strain was computed among all nodes inside the applied pressure region (figure 5). Simulated strain results were able to predict the deformation of the pressure sensor made of viscoelastic material, with an average strain of ≈11% for a maximum applied pressure of 1 MPa.

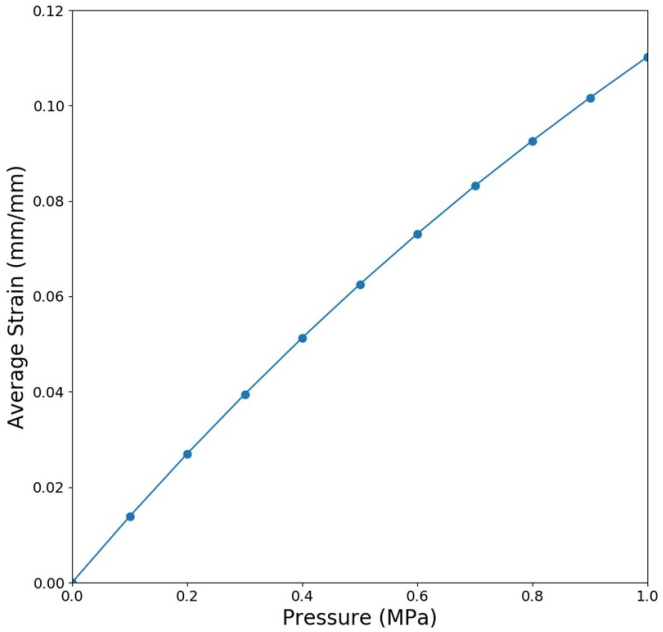

Figure 5. Pressure versus strain (in the normal direction) plot obtained from the FEA simulation results. The strain values correspond to the average strain among all nodes inside the applied load region (172 nodes).

4. Experimental setup and results

4.1. Experimental setup

A testing rig was built for conditioning and characterizing the microfluidic pressure sensors. We used a pneumatic cylinder (1.06DPSR02.0, Parker Hannifin) with a bore diameter of 1.0625 inches (≈27 mm) and rod diameter of 0.3125 inches (≈8 mm) and mounted to a rigid frame in a vertical position. A custom-built metallic force concentrator (6061 Aluminum) of 16 mm in diameter (64% of sensor active area) was threaded to its rod end in order to distribute the applied pressure over the sensor top surface. The sensor was bonded to a flat surface under the air cylinder rod end (figure 6). A miniaturized pneumatic controller board was used to control the pressure of a compressed air pipeline source. The source maximum pressure was set to 80 psi with a pneumatic filter regulator. The air pressure at the pneumatic cylinder was controlled by a solenoid valve (VQ110U-6M, SMC USA) connected to a MOSFET switch, which was modulated via a programmable microcontroller (Arduino Mega 2560, Arduino) using a PID controller for pressure setpoint tracking. Sensor measurements were collected using a voltage divider circuit ($R_{\text{ref}} = 47\ \Omega$) and connected to the same programming board using its analog-to-digital converter pins with the default internal voltage of 5 V (figure 7). Two insulated copper test leads with alligator clips were used to connect the pressure sensor terminals to the voltage divider circuit. All sensor data was recorded via serial communication using a Python script running on a workstation computer during both conditioning and characterization procedures. The total pressure at the sensor top surface, P_{surf}, was determined by

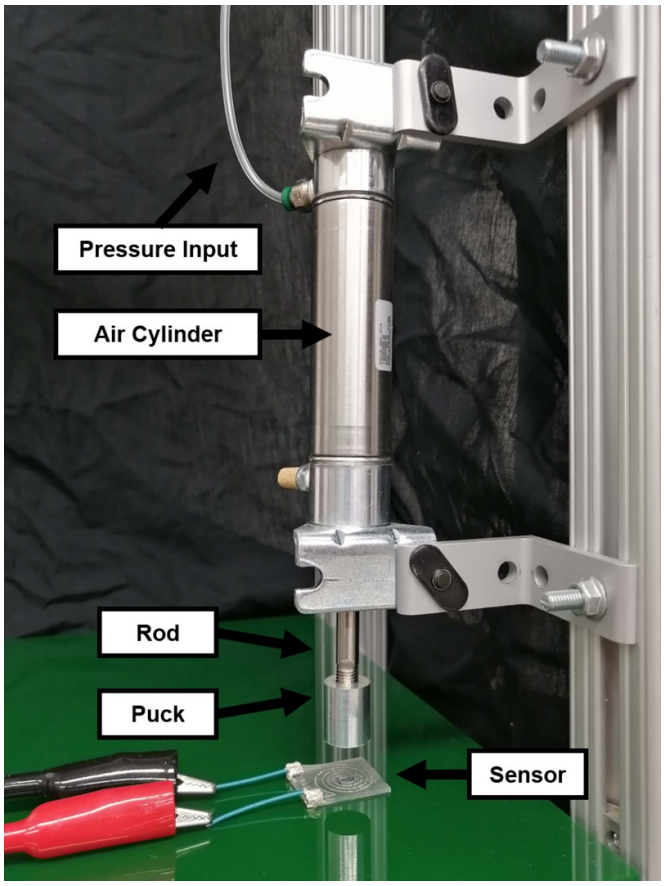

Figure 6. Test rig for measuring and characterizing the 3D-printed pressure sensors, with a vertically mounted fluidic cylinder with custom-built force concentrator (16 mm diameter) controlled by a pneumatic power source.

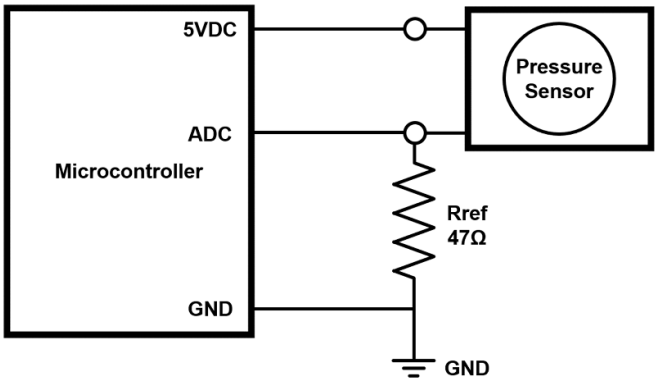

Figure 7. An electrical schematic of the voltage divider circuit for collecting pressure sensor measurements.

$$P_{\text{surf}} = \frac{P_{\text{gauge}} \times A_{\text{bore}}}{A_{\text{puck}}} = \frac{F_{\text{rod}}}{2.01 \times 10^{-4}\,\text{m}^2} \tag{3}$$

where P_{gauge} is the total pressure inside the air cylinder, A_{bore} is the bore area, A_{puck} is the area of the force concentrator, and F_{rod} is the force generated at the rod.

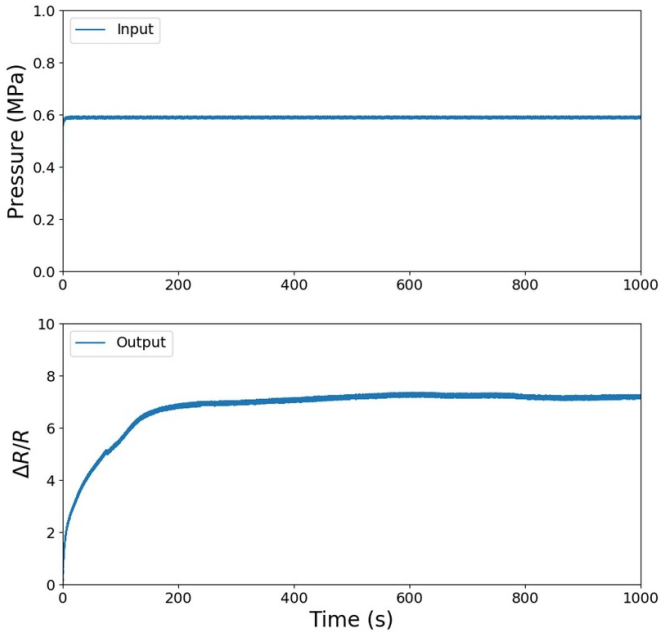

Figure 8. Step response collected from the pressure sensor for a constant input of 0.6 MPa. The top graph shows the input pressure and the bottom graph shows the measured relative change in resistance.

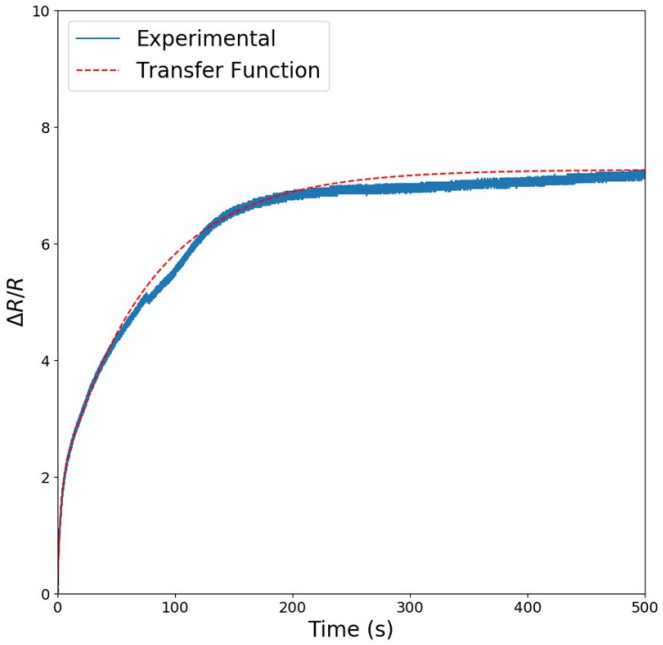

Figure 9. Comparison of a step response for both the experimental data and the obtained transfer function through model fitting.

4.2. Step response

The relative change in electrical resistance of the 3D-printed microchannel filled with liquid conductor, $\Delta R/R$, was recorded as a function of the generated pressure at the force concentrator, P_{surf}. The sensor response was first evaluated by applying a step signal of 30 psi at the gauge ($P_{\text{surf}} = 0.6$ MPa). The obtained experimental result shows that the sensor can quickly respond to the pressure input, but then takes about 500 seconds to reach the steady-state, with $\Delta R/R \approx 7.2$ as shown in figure 8. This observed creep can be partly explained by the viscoelasticity of the 3D-printed resin material as discussed in [47].

Further computational study was performed to identify a model with these intrinsic characteristics. The sensor data obtained during the step response experiment was imported in a software (MATLAB, Mathworks) to estimate a transfer function model. Equation (4) shows the estimated transfer function model from the time-domain data with a fit to estimated data of 93.23% and represented as a second order system with two poles (-0.4382 and -0.0134) and one zero (-0.0505):

$$G(s) = \frac{\Delta R/R}{P_{\text{surf}}} = \frac{1.406\, s + 0.07097}{s^2 + 0.4516\, s + 0.005858}. \qquad (4)$$

In figure 9, we can observe a good match between the experimental data and the model-predicted step response. The two poles of the system (4) suggest two disparate modes, with time constants of 9.1 s and 298.5 s, respectively.

Although the electrical characteristics of the sensor have not been investigated during the simulation analysis in section 3, the resistance of the sensor output was collected at different pressure values for further correlational study between simulation and experimental results. In order to measure the sensor resistance close to steady-state regime at multiple pressures, a staircase pressure signal with increment size of 0.1 MPa and duration of 2000 s per step was applied to the control board. An average value for the relative change in resistance at each pressure step was computed for a range of 100 points along the steady-state regime (figure 10). By combining the simulation results from figure 5 with the experimental results from figure 10, we can derive the correlation between the pressure sensor average strain inside the load region and the observed relative change in resistance for a given applied pressure value (figure 11). One can observe that the sensitivity of the device increases with the applied pressure. For example, from figure 11, the gauge factor of the sensor, evaluated as the slope of the plot, is around 1000 when the strain is over 0.08.

4.3. Sinusoidal responses

To further analyze the dynamic response of the sensor, sinusoidal pressure stimuli were generated with frequencies $f_s =$ 0.1 Hz, 0.25 Hz, 0.5 Hz and 1 Hz, bias of 30 psi and amplitude of 20 psi at the gauge (0.2 MPa $< P_{\text{surf}} <$ 0.977 MPa). Note that the choice of the pressure input (in particular the bias value for the cyclic input) allows the sensor to stay away from the low-response regime (below 0.2 MPa; see figure 10), so that we can better examine the consistency and behavior under the cyclic input. Figure 12 shows the relative change in resistance when this cyclic signal was applied for a period of 2000 seconds at each frequency value. A mean curve shows the average values of $\Delta R/R$ computed at each respective T_s cycle. A close view of each measurement is shown in figure 13. The particular creep phenomenon is still observed under the cyclic inputs, and the time it takes the mean curve to reach the steady

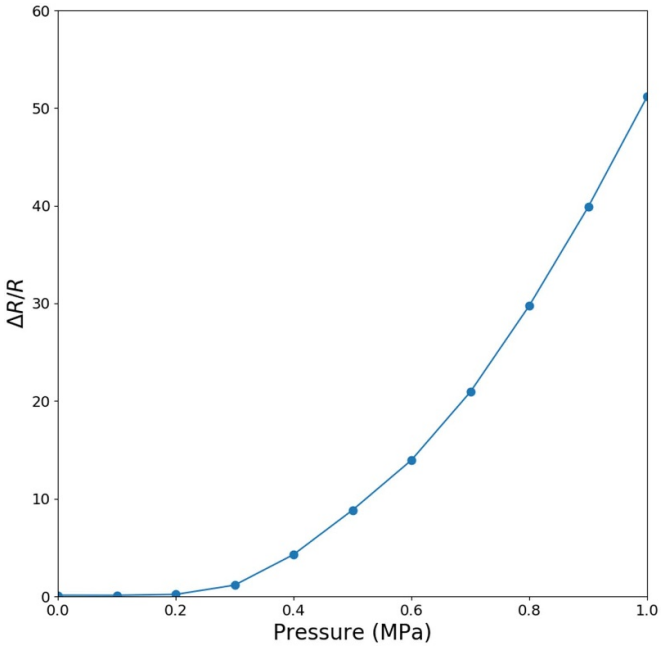

Figure 10. The relative change in resistance versus the pressure input for a staircase input signal. The average value of $\Delta R/R$ was computed for a range of 100 points along the steady-state regime, with a pressure input from 0 to 1 MPa, increment size of 0.1 MPa, and duration of 2000 s per step.

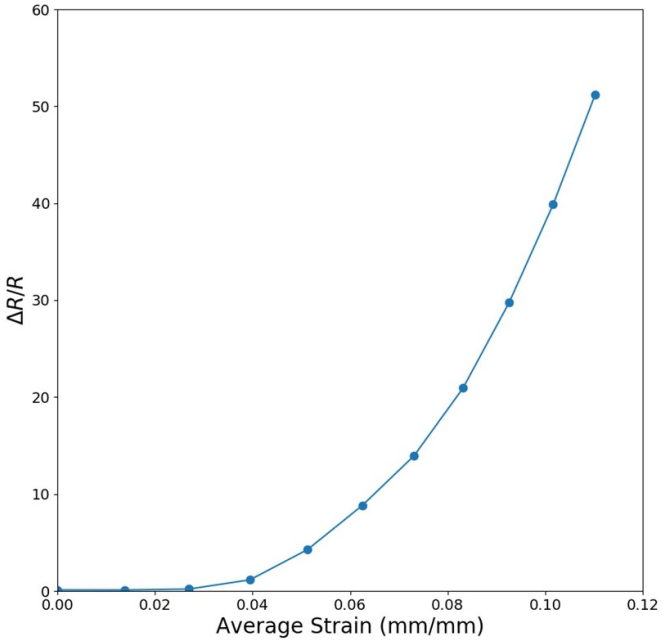

Figure 11. The correlation between the computed average strain from FEA simulation at the sensor active area and the relative change in resistance measured from the physical pressure sensor device.

state is comparable to the case of a quasi-static input (figure 8). The sensor output versus pressure graphs on figure 14 were generated by capturing the relative change in resistance after the sensor has reached its steady-state regime (>1000 s). From these results, it can be seen that the sensor behavior is largely

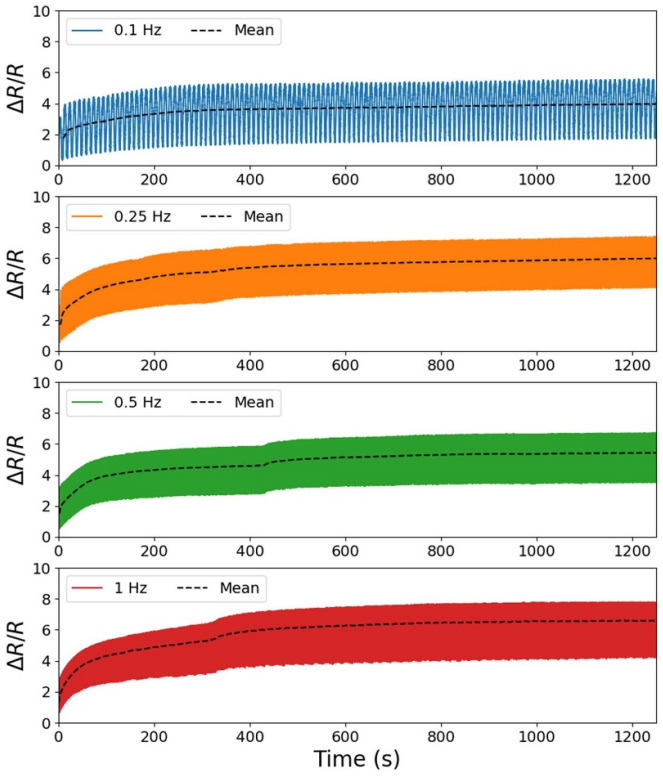

Figure 12. Full cycle of each sinusoidal input with its respective frequency. The dashed lines show the mean curve of the continuous measurements.

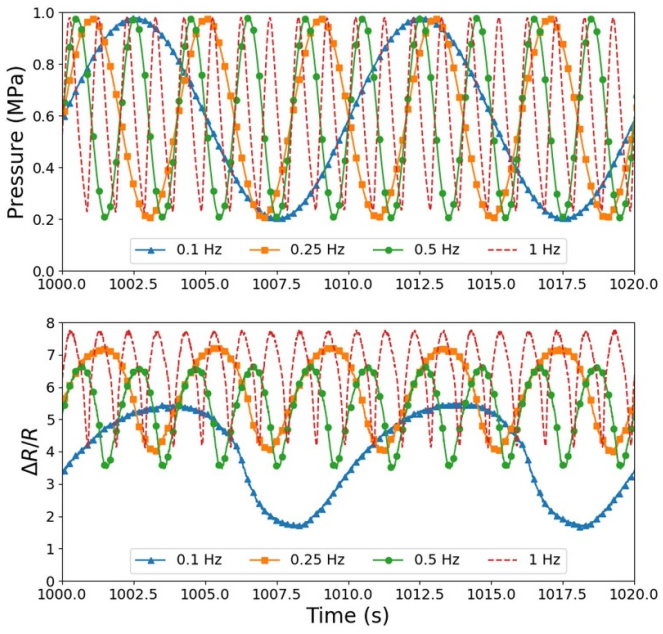

Figure 13. Sinusoidal response for multiple input frequencies (frame view of 20 s). Each measurement was collected for >2000 s at 0.1 Hz, 0.25 Hz, 0.5 Hz, and 1 Hz, with a pressure range of 0.2 MPa to 0.977 MPa.

repeatable under cyclic inputs. In addition, the dynamic behavior shows dependence on the stimulus frequency. As the frequency increases, the mean range of the sensor output tends

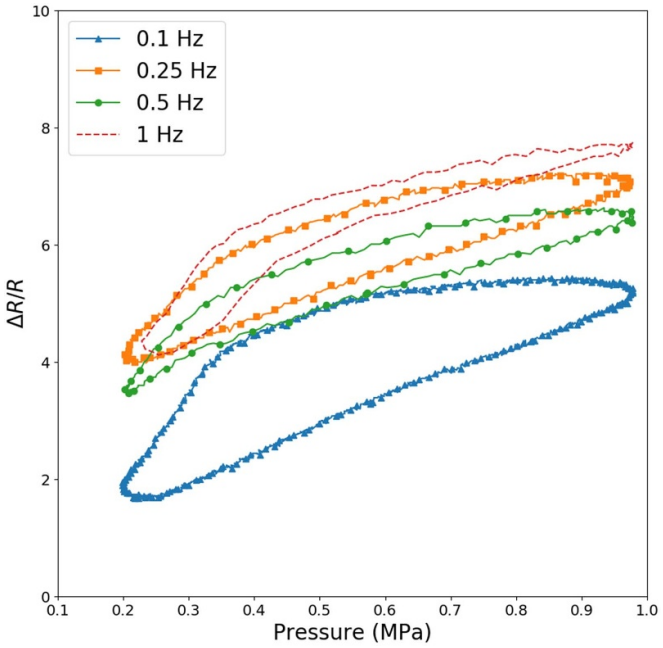

Figure 14. Sensor output–input graphs under pressure inputs of different frequencies.

to align. It is also interesting to note that the loops in the resistance-change versus pressure graphs become narrower as the frequency increases. The latter can be considered a rate-dependent hysteresis behavior [48]. Hysteresis itself is characterized by a non-trivial loop in the steady-state output vs input graph of the system when the input is varied periodically and quasi-statically [49]. In reality the shape of the output vs input loop often varies with the input frequency [48, 50] due to the coupling of hysteresis effect with other dynamics in the system. In the case of our sensor, we conjecture that both the viscoelasticity of the 3D-printed substrate and the dynamic interaction between the liquid metal and the micro-channels contribute to the observed rate-dependent hysteresis, which will be examined in our future work.

5. Discussions

Dispersion of the liquid sacrificial material is still a challenging process in the fabrication technique presented here, since accidental formation of beads can cause clogging or irregular structure design of the microfluidic channels. Moreover, the manual removal of the liquid support material through suction with a vacuum pump, and the manual injection of liquid metal using syringes have varied fabrication time due to non-uniform tool manipulation and material handling. A way to improve our fabrication method would be to make these procedures automated by the same 3D-printing mechanism.

The intrinsic viscoelasticy of the rubber-like photocurable material has shown some impact on the soft pressure sensor response time, taking several hundred seconds for the sensor to reach a steady-state regime. Additional investigations on substrates made of different mixing ratios between soft and rigid 3D-printable photopolymers and overall thicknesses are required in order to analyze their impact on the sensor performance.

Encapsulation of the pressure sensor inlets was performed by using silver epoxy as an interface between the liquid conductor and copper stranded wires. Other methods have been tested initially such as deposition of uncured Agilus30 on the sensor terminals with thin copper wires attached at each end, and curing process using UV-light flashlight. However, poor quality deposition or curing caused leakage of the liquid metal when subjecting the sensor to very high pressure values. 3D-printing of an encapsulation layer was also tested, but the attached thin wires and the liquid metal exposed surface made it a challenging process due to blockage or undesired contamination of the printer head. While the selected silver epoxy showed great adhesion and encapsulation properties, further study is needed to analyze its effect on the sensor characteristics. Also, the surface oxide skin on a liquid metal can affect the effective surface tension and viscosity (non-spherical droplets formation), which can reduce its contact with other materials and potentially impact its electrical properties.

Simulation results of the pressure sensor have shown that consistent FEM results can be obtained when certain rules are followed, like using hexahedral elements to improve convergence and enhance accuracy of the computed strain fields. Similar deformations were observed in both simulation and experiments during cyclic input pressure, including a bulging effect around the circular deformed region due to the intrinsic hyperelastic characteristics of the 3D-printed material. However, since the FEM simulation in this work did not include the microchannel cavities and liquid metal material, further investigation is required to completely analyze their impact on the computed average strain value.

6. Conclusions

This work presented a novel method for achieving 3D-printed stretchable pressure sensors and conductors using liquid metal as a circuit component. A PolyJet 3D-printer was used to create a microchannel structure inside the soft substrate in combination with a viscous liquid mixture for sacrificial layer. Functional straight-shaped microchannels were fabricated with sizes down to 150 $\times$ 150 μm of cross-section area. A spiral shaped pressure sensor was designed with 350 $\times$ 350 μm microchannel cross-section and manually injected with liquid metal using a syringe. Experimental results showed that the multimaterial-based sensor with mixture of Agilus30 and VeroClear (70A Shore Hardness) and overall thickness of 1.5 mm was able to withstand high pressures up to 1 MPa. This made the pressure sensor suitable for applications that require resistance to very high deformations such as in modern electronics for several fields and industry, including wearable or implantable devices, military and soft robotics.

While major challenges still exist, such 3D-printed devices with material properties allowing large-strain deformations can provide a new generation of sensors and conductors

achieved with rapid manufacturing technologies for fast delivery to the market. Future work will include the analysis of multiple microchannel cross-section sizes and substrate overall thickness to further investigate how these parameters can affect the sensor performance. Furthermore, we will develop an improved model that can capture the viscoelasticity characteristics of the 3D-printed material and the microfluidic flow of the embedded liquid metal, which will be instrumental in design and optimization of the dynamic behavior of the sensor. In particular, we plan to use microscopic imaging to observe the movement of liquid metal (including its possible infiltration into the substrate) and understand its dynamics in interacting with the substrate during variation of the applied pressure.

Data availability statement

All data that support the findings of this study are included within the article (and any supplementary files).

Acknowledgments

We would like to thank the 3D-Printing Core Facility from The Institute for Quantitative Health Science and Engineering (IQ Building) at Michigan State University for providing the necessary resources for this research work.

This work was supported by Coordenação de Aperfeiçoamento de Pessoal de Nível Superior (CAPES), National Science Foundation (DBI-0939454C and CMMI-1940950) and an MSU Strategic Partnership Grant (16-SPG-Full-3236)

ORCID iD

Thassyo Pinto https://orcid.org/0000-0002-3964-8280

References

[1] Whitesides G M 2006 The origins and the future of microfluidics *Nature* **442** 368
[2] Vogt D M, Park Y-L and Wood R J 2013 Design and characterization of a soft multi-axis force sensor using embedded microfluidic channels *IEEE Sens. J.* **13** 4056–64
[3] Chossat J-B, Shin H-S, Park Y-L and Duchaine V 2015 Soft tactile skin using an embedded ionic liquid and tomographic imaging *J. Mech. Rob.* **7** 021008
[4] Chossat J-B, Park Y-L, Wood R J and Duchaine V 2013 A soft strain sensor based on ionic and metal liquids *IEEE Sens. J.* **13** 3405–14
[5] Schubert B E and Floreano D 2013 Variable stiffness material based on rigid low-melting-point-alloy microstructures embedded in soft poly (dimethylsiloxane)(PDMS) *RSC Adv.* **3** 24671–9
[6] Zarifi M H, Sadabadi H, Hejazi S H, Daneshmand M and Sanati-Nezhad A 2018 Noncontact and nonintrusive microwave-microfluidic flow sensor for energy and biomedical engineering *Sci. Rep.* **8** 1–10
[7] Koh A *et al* 2016 A soft, wearable microfluidic device for the capture, storage and colorimetric sensing of sweat *Sci. Trans. Med.* **8** 366ra165–366ra165
[8] Choi J, Kang D, Han S, Kim S B and Rogers J A 2017 Thin, soft, skin-mounted microfluidic networks with capillary bursting valves for chrono-sampling of sweat *Adv. Healthcare Mater.* **6** 1601355
[9] Choi J, Ghaffari R, Baker L B and Rogers J A 2018 Skin-interfaced systems for sweat collection and analytics *Sci. Adv.* **4** eaar3921
[10] Pinto T, Cai L, Wang C and Tan X 2017 CNT-based sensor arrays for local strain measurements in soft pneumatic actuators *Int. J. Intell. Robot. Appl.* **1** 157–66
[11] Shi H, Al-Rubaiai M, Holbrook C M, Miao J, Pinto T, Wang C and Tan X 2019 Screen-printed soft capacitive sensors for spatial mapping of both positive and negative pressures *Adv. Funct. Mater.* **29** 1809116
[12] Coleman D, Al-Rubaiai M and Tan X 2019 Temperature-compensation of 3d-printed polymer-based strain gauges *Behavior and Mechanics of Multifunctional Materials Xiii Int. Society for Optics and Photonics* **10968** 109680M
[13] Al-Rubaiai M, Pinto T, Qian C and Tan X 2019 Soft actuators with stiffness and shape modulation using 3D-printed conductive polylactic acid material *Soft Robot.* **6** 318–32
[14] Lu N and Kim D-H 2014 Flexible and stretchable electronics paving the way for soft robotics *Soft Robotics* **1** 53–62
[15] Qi D, Zhang K, Tian G, Jiang B and Huang Y 2020 Stretchable electronics based on PDMS substrates *Adv. Mater.* **33** 2003155
[16] Wu H, Odom T W, Chiu D T and Whitesides G M 2003 Fabrication of complex three-dimensional microchannel systems in PDMS *J. Am. Chem. Soc.* **125** 554–9
[17] Wang X, Guo R and Liu J 2019 Liquid metal based soft robotics: materials, designs and applications *Advanced Materials Technologies* **4** 1800549
[18] Dickey M D, Chiechi R C, Larsen R J, Weiss E A, Weitz D A and Whitesides G M 2008 Eutectic gallium-indium (EGaIn): a liquid metal alloy for the formation of stable structures in microchannels at room temperature *Adv. Funct. Mater.* **18** 1097–104
[19] Dickey M D 2017 Stretchable and soft electronics using liquid metals *Adv. Mater.* **29** 1606425
[20] Mengüç Y, Park Y-L, Martinez-Villalpando E, Aubin P, Zisook M, Stirling L, Wood R J and Walsh C J 2013 Soft wearable motion sensing suit for lower limb biomechanics measurements *2013 IEEE Int. Conf. on Robotics and Automation* (IEEE) pp 5309–16
[21] Mengüç Y *et al* 2014 Wearable soft sensing suit for human gait measurement *Int. J. Robot. Res.* **33** 1748–64
[22] Chossat J-B, Tao Y, Duchaine V and Park Y-L 2015 Wearable soft artificial skin for hand motion detection with embedded microfluidic strain sensing *2015 IEEE Int. Conf. on Robotics and Automation (ICRA)* (IEEE) pp 2568–73
[23] Hammond F L, Kramer R K, Wan Q, Howe R D and Wood R J 2014 Soft tactile sensor arrays for force feedback in micromanipulation *IEEE Sens. J.* **14** 1443–52
[24] Park Y-L and Wood R J 2013 Smart pneumatic artificial muscle actuator with embedded microfluidic sensing *Sensors, 2013 IEEE* (IEEE) pp 1–4
[25] Morrow J, Shin H-S, Phillips-Grafflin C, Jang S-H, Torrey J, Larkins R, Dang S, Park Y-L and Berenson D 2016 Improving soft pneumatic actuator fingers through integration of soft sensors, position and force control and rigid fingernails *2016 IEEE Int. Conf. on Robotics and Automation (ICRA)* (IEEE) pp 5024–31
[26] Hao Y, Wang T, Xie Z, Sun W, Liu Z, Fang X, Yang M and Wen L 2018 A eutectic-alloy-infused soft actuator with sensing, tunable degrees of freedom and stiffness properties *J. Micromech. Microeng.* **28** 024004
[27] Ladd C, So J-H, Muth J and Dickey M D 2013 3d printing of free standing liquid metal microstructures *Adv. Mater.* **25** 5081–5

[28] Boley J W, White E L, Chiu G T-C and Kramer R K 2014 Direct writing of gallium-indium alloy for stretchable electronics *Adv. Funct. Mater.* **24** 3501–7
[29] Parekh D P, Ladd C, Panich L, Moussa K and Dickey M D 2016 3D printing of liquid metals as fugitive inks for fabrication of 3D microfluidic channels *Lab on a Chip* **16** 1812–20
[30] Prakash S and Kumar S 2015 Fabrication of microchannels: a review *Proc. Inst. Mech. Eng., Part B: J. Eng. Manuf.* **229** 1273–88
[31] Paik J K, Kramer R K and Wood R J 2011 Stretchable circuits and sensors for robotic origami *2011 IEEE/RSJ Int. Conf. on Intelligent Robots and Systems* (IEEE) pp 414–20
[32] Majidi C, Kramer R and Wood R 2011 A non-differential elastomer curvature sensor for softer-than-skin electronics *Smart Mater. Struct.* **20** 105017
[33] Park Y-L, Majidi C, Kramer R, Bérard P and Wood R J 2010 Hyperelastic pressure sensing with a liquid-embedded elastomer *J. Micromech. Microeng.* **20** 125029
[34] Jo B-H, Van Lerberghe L M, Motsegood K M and Beebe D J 2000 Three-dimensional micro-channel fabrication in polydimethylsiloxane (PDMS) elastomer *J. Microelectromech. Syst.* **9** 76–81
[35] Park Y-L, Chen B-R and Wood R J 2012 Design and fabrication of soft artificial skin using embedded microchannels and liquid conductors *IEEE Sens. J.* **12** 2711–18
[36] Kramer R K, Majidi C, Sahai R and Wood R J 2011 Soft curvature sensors for joint angle proprioception *2011 IEEE/RSJ Int. Conf. on Intelligent Robots and Systems* (IEEE) pp 1919–26
[37] Habibey R, Golabchi A, Latifi S, Difato F and Blau A 2015 A microchannel device tailored to laser axotomy and long-term microelectrode array electrophysiology of functional regeneration *Lab on a Chip* **15** 4578–90
[38] Au A K, Huynh W, Horowitz L F and Folch A 2016 3D-printed microfluidics *Angew. Chem., Int. Ed.* **55** 3862–81
[39] Amin R, Knowlton S, Hart A, Yenilmez B, Ghaderinezhad F, Katebifar S, Messina M Khademhosseini A and Tasoglu S 2016 3D-printed microfluidic devices *Biofabrication* **8** 022001
[40] Alfadhel A, Ouyang J, Mahajan C G, Forouzandeh F, Cormier D and Borkholder D A 2018 Inkjet printed polyethylene glycol as a fugitive ink for the fabrication of flexible microfluidic systems *Mater. Des.* **150** 182–7
[41] Emon M O F, Alkadi F, Philip D G, Kim D-H, Lee K-C and Choi J-W 2019 Multi-material 3d printing of a soft pressure sensor *Additive Manuf.* **28** 629–38
[42] Castiaux A D, Pinger C, Hayter E A, Bunn M E, Martin R S and Spence D M 2019 Polyjet 3D-printed enclosed microfluidic channels without photocurable supports *Anal. Chem.* **91** 6910–17
[43] Park Y-L, Chen B-R and Wood R J 2011 Soft artificial skin with multi-modal sensing capability using embedded liquid conductors *Sensors, 2011 IEEE* (IEEE) pp 81–4
[44] Shin H-S, Ryu J, Majidi C and Park Y-L 2016 Enhanced performance of microfluidic soft pressure sensors with embedded solid microspheres *J. Micromech. Microeng.* **26** 025011
[45] Chiechi R C, Weiss E A, Dickey M D and Whitesides G M 2008 Eutectic gallium–indium (EGaIn): a moldable liquid metal for electrical characterization of self-assembled monolayers *Angew. Chem., Int. Ed.* **47** 142–4
[46] Abayazid F F and Ghajari M 2020 Material characterisation of additively manufactured elastomers at different strain rates and build orientations *Additive Manuf.* **33** 101160
[47] Dykstra D M, Busink J, Ennis B and Coulais C 2019 Viscoelastic snapping metamaterials *J. Appl. Mech.* **86** 111012
[48] Iyer R V and Tan X 2009 Control of hysteretic systems through inverse compensation *IEEE Control Syst. Mag.* **29** 83–99
[49] Drinčić B, Tan X and Bernstein D S 2011 Why are some hysteresis loops shaped like a butterfly? *Automatica* **47** 2658–64
[50] Tan X and Baras J S 2004 Modeling and control of hysteresis in magnetostrictive actuators *Automatica* **40** 1469–80